

Prethermal Floquet steady-states and instabilities in the periodically-driven, weakly-interacting Bose-Hubbard model

Marin Bukov,^{1,*} Sarang Gopalakrishnan,² Michael Knap,^{2,3} and Eugene Demler²

¹*Department of Physics, Boston University, 590 Commonwealth Ave., Boston, MA 02215, USA*

²*Department of Physics, Harvard University, 17 Oxford Street, Cambridge, MA 02138, USA*

³*Physik Department and Walter Schottky Institut,
Technische Universität München, 85748 Garching, Germany*

(Dated: March 26, 2025)

We explore the prethermal Floquet steady-states and instabilities of the weakly interacting two-dimensional Bose Hubbard model subject to periodic driving. We develop a description of the nonequilibrium dynamics using a weak-coupling conserving approximation. This approach allows us to explore dynamics at arbitrary drive strength and frequency. We establish the regimes in which conventional (zero-momentum) and unconventional ((π, π) -momentum) condensates are stable on intermediate time scales. We find that the condensate stability is *enhanced* by increasing the drive strength, because this decreases the bandwidth of quasiparticle excitations and thus impedes resonant absorption and heating. Our results are directly relevant to a number of current experiments with ultracold lattice bosons.

Periodically driven systems^{1,2} often exhibit exotic phenomena that are absent in their non-driven counterparts. Classic examples include the Kapitza pendulum and the periodically kicked rotor. More recently, periodically driven optical lattices have attracted interest as a way of controlling single-particle hopping^{3–9} in order to engineer gauge fields^{10–16}, topological band structures^{17–22}, and associated exotic states of matter. The existence of such exotic states is established in noninteracting systems and in certain mean-field models; the extent to which they survive in the presence of interactions is a central open question. It is believed, from the eigenstate thermalization hypothesis^{23–25}, that driven interacting systems will generically heat up to infinite temperature at sufficiently late times, as a result of resonant energy absorption from the drive^{26–29}. Even if heating occurs at late times, however, in some parameter regimes these times will be parametrically slower than the characteristic timescales of the system. In that case, the system will rapidly approach a “prethermalized” Floquet steady state^{30,31}, which governs the dynamics until the much later times at which heating becomes effective.

In the present work, we explore these intermediate-time steady states for the case of the weakly interacting, two-dimensional (2D), periodically-driven Bose-Hubbard model (BHM). The regime we explore is directly relevant to experiments^{5,6,9,12–14,16,20}, where often weak interactions are unavoidable due to a lack of a controllable Feshbach resonance. We describe this regime using a self-consistent weak-coupling conserving approximation (WCCA) which treats the coupled nonlinear dynamics of the condensate and the quasiparticle spectrum while neglecting collisions between quasiparticles. This approximation is justified at weak interaction strengths because the nonlinear couplings are important at much shorter times than the collisional timescales.

Within the WCCA, we find a phase diagram (Fig. 1) featuring at low drive frequency a regime in which the superfluid state is *already* unstable at lowest order in

the interactions, owing to the resonant creation of quasiparticle pairs, and a regime (at high drive frequency) where the superfluid is stable. In the WCCA, there is a sharp phase transition between these regimes; when effects beyond weak coupling are included, there will be a qualitative difference in heating rates. Thus, in the “stable” regions of Fig. 1, the system initially reaches a prethermalized superfluid state—featuring a nonequilibrium quasiparticle distribution—and then eventually

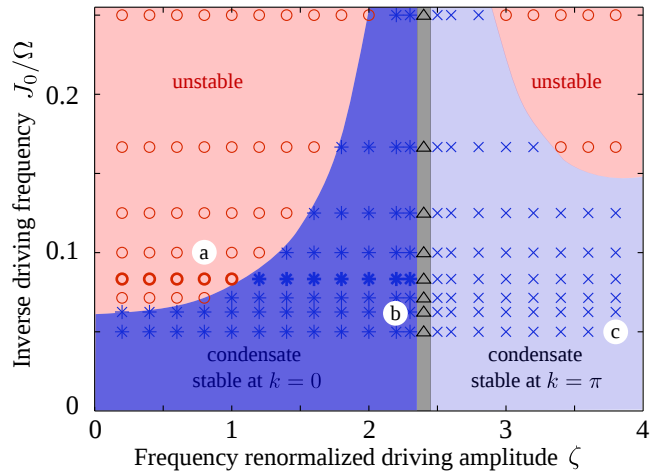


FIG. 1: (Color online) Stability diagram of the driven Bose-Hubbard model for $U/J_0 = 0.2$. In the pink regions the condensate is unstable as the drive parametrically excites pairs of phonons in the superfluid. In contrast, in the blue regions the condensate is stable on the intermediate time scales of the prethermal Floquet regime. In the grey shaded region around $\zeta \approx 2.405$ the system is strongly correlated (see text). The symbols are determined from the numerical solution of the self-consistent weak-coupling conserving approximation over 801 driving cycles; the boundaries are given by the analytical expression Eq. (5). The letters (a), (b), (c) correspond to the subplots in Fig. 3.

heats up and loses coherence. For strong driving, the prethermalized superfluid state is exotic, involving condensation at momentum $\boldsymbol{\pi} = (\pi, \pi)$. The existence of this exotic phase in the high-frequency limit has previously been established^{4,6}; we find that this effect persists for intermediate frequencies as well.

Remarkably, we find that the stable phase is *enhanced* for intermediate drive strengths. Physically, this occurs because the drive has two effects: first, it creates quasiparticle pairs when this is a resonant process; and second, it decreases the effective hopping rate and thus the effective bandwidth of quasiparticle excitations. This latter effect is well understood in the infinite-frequency limit, where the dynamics is described by an effective time-averaged Hamiltonian^{3,4,6}. A key conclusion of our work is that, for weak interactions but general drive amplitude and frequency, the condensate becomes unstable when the drive frequency is parametrically resonant with the *drive-renormalized* effective bandwidth. Therefore, parametric resonance occurs at *lower* frequencies when the drive strength is ramped up.

Model.—We consider the Bose-Hubbard model (BHM) on a square lattice in the presence of a circularly polarised time-periodic force $\mathbf{E}(t) = A(\cos \Omega t, \sin \Omega t)^T$:

$$H_{\text{lab}}(t) = -J_0 \sum_{\langle ij \rangle} b_i^\dagger b_j + \frac{U}{2} \sum_j n_j(n_j - 1) + \sum_j \mathbf{E}(t) \cdot \mathbf{r}_j n_j. \quad (1)$$

The operator b_j^\dagger (b_j) creates (destroys) a boson on lattice site $j = (m, n)$. The tunnelling matrix element and the interaction strength are denoted by J_0 and U , respectively, and the lattice position vector is defined as $\mathbf{r}_j = (m, n)$. In order to achieve non-trivial dynamics in the high-frequency regime, we scale the driving amplitude linearly with the driving frequency $A \sim \Omega$.² Therefore, we assume that the ratio $\zeta = A/\Omega$ can be controlled independently of Ω . We eliminate the divergent amplitude $A \sim \Omega$ by a local unitary transformation to a rotating frame (cf. App. A), after which the Hamiltonian reads

$$H(t) = -J_0 \sum_{\langle ij \rangle} e^{i\mathcal{A}(t) \cdot (\mathbf{r}_i - \mathbf{r}_j)} b_i^\dagger b_j + \frac{U}{2} \sum_j n_j(n_j - 1). \quad (2)$$

Thus, in the rotating frame, the system experiences an effective time-dependent gauge potential $\mathcal{A}(t) = \zeta(\sin \Omega t, -\cos \Omega t)^T$. The time evolution of $U(1)$ -invariant quantities remains the same in both frames. It has been shown that for such quantities, one can rely on stroboscopic evolution to describe their dynamics unambiguously³². From now on, we shall focus on the rotating frame explicitly. The unitary transformation to the rotating frame does not change the stability properties of the system.

Weak-coupling conserving approximation (WCCA). To study the driven system at arbitrary frequencies, we employ a self-consistent, weak-coupling conserving approximation. In technical terms, the WCCA involves deriving equations of motion from a two-particle irreducible effective action³³ within the nonequilibrium Schwinger-Keldysh formalism, but keeping only diagrams to first order in U (see App. B). Our motivation for using this approach is that, unlike simple perturbation theory or Bogoliubov theory, the WCCA respects unitarity and conservation laws³⁴, and thus gives physically sensible results for all times. While the WCCA is *not* guaranteed to yield a gapless excitation spectrum^{34,35}, the precise low-frequency behavior of the excitation spectrum is not relevant for the nonequilibrium phenomena discussed here. Our approach is equivalent to a fully self-consistent, time-dependent Hartree-Fock-Bogoliubov (HFB) approximation^{35,36}; our field theoretic formulation, however, can more readily be extended to higher orders in U . The WCCA can be understood physically as follows. In the general nonequilibrium problem, the dynamics of the condensate and the Bogoliubov quasiparticles are coupled: the Bogoliubov equations depend explicitly on the condensate, while the condensate depends on the Bogoliubov spectrum via particle number conservation. To study nonequilibrium dynamics while allowing for the condensate to deplete with time, one must include both processes. Crucially, this allows the exponential growth of unstable modes to be cut off by the resulting depletion of the condensate. The minimal approximation that achieves this, while respecting all conservation laws, is the WCCA.

The equations of motion using the WCCA are derived as shown in App. B, and then solved numerically. For the results presented here, we prepared the system at time $t = 0$ on a $N_s = 100 \times 100$ lattice in the ground state of Bogoliubov theory, which is expected to describe the equilibrium physics well for weak interactions in 2D. We allow for a macroscopic population of the $\mathbf{k} = \boldsymbol{\pi}$ mode to include the possibility of a condensate at momentum $\boldsymbol{\pi}$. The initial condition for the condensate fractions is chosen to be $|\varphi_{k=0}|^2 = n_0$ for $\zeta < 2.405$ and $|\varphi_{k=\pi}|^2 = n_0$ for $\zeta > 2.405$, where n_0 is the total condensate fraction for the non-driven model in Bogoliubov theory. To study the nonequilibrium dynamics, we abruptly turn on the periodic drive and propagate the initial state for several hundred driving cycles using Eqs. (B14) and (B15). We checked that the results are insensitive to system size.

Stability diagram.—The stability phase diagram is shown in Fig. 1. Previous work has investigated the stability of the Bose-Hubbard model³⁷ and related models^{38–40} using various approximation schemes; we go beyond these works by treating both the condensate and the quasiparticle sectors, and including the feedback between them. Thus, we are able to explore instabilities originating in either sector on equal footing.

We first discuss two analytically tractable limits, corresponding to high-frequency driving (i.e., going along

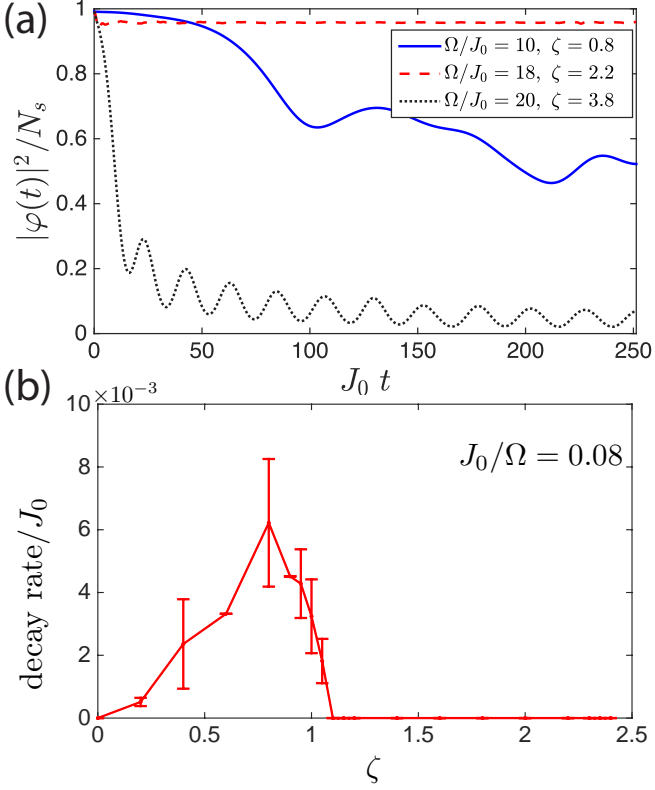


FIG. 2: (Color online). (a) Time evolution of the condensate fraction for 801 driving cycles, starting from a Bogoliubov initial state localised at $\mathbf{k} = \mathbf{0}$ for $U/J_0 = 0.2$. (b) Decay rate to 75% of the condensate curves for $\Omega/J_0 = 12$ (bold-face points in Fig. 1). To take into account the oscillatory behaviour, the error bars are set by the difference of the inverse times corresponding to the first and last time the curve passes through 3/4.

the x axis of Fig. 1) and to low-amplitude driving (i.e., going along the y axis). The dynamics is then governed by an effective *time-averaged* Hamiltonian^{1,2}:

$$H_F \approx -J_{\text{eff}}(\zeta) \sum_{\langle ij \rangle} b_i^\dagger b_j + \frac{U}{2} \sum_j n_j(n_j - 1). \quad (3)$$

As a consequence of the periodic modulation, the hopping amplitude is renormalised to $J_{\text{eff}}(\zeta) = J_0 \mathcal{J}_0(\zeta)$, where $\mathcal{J}_0(\zeta)$ is the zeroth-order Bessel function of the first kind, which is a damped oscillatory function with the first zero at $\zeta \approx 2.4$, the second at $\zeta \approx 5.5$, etc. Thus, as ζ is increased, the effective hopping decreases, until the dispersion flattens at $\zeta \approx 2.4$. For $\zeta > 2.4$ the dispersion flips sign, and acquires a stable minimum at $\pi = (\pi, \pi)$. Thus, one expects that in the high-frequency limit the condensate at $\mathbf{0} = (0, 0)$ is stable when $\zeta < 2.4$ and unstable otherwise, whereas the condensate at π is stable when $2.4 \lesssim \zeta \lesssim 5.5$. This agrees with what we find numerically. Moreover, for commensurate filling, the superfluid phase should transition into a Mott insulating state around $\zeta = 2.4$ determined by the phase

boundary $J_{\text{eff}}(\zeta)/U \lesssim 0.06$.^{41,42} This transition regime, marked by the thin vertical strip in Fig. 1, is beyond the regime of validity of the WCCA; our WCCA simulations in this regime give oscillatory behavior, discussed in Appendix D.

A second analytically tractable limit is that of weak driving, at arbitrary Ω . The effects of such a weak drive can be inferred from linear stability analysis around the non-driven state (or, equivalently, from the Golden Rule). In terms of Bogoliubov quasiparticle operators γ , the system-drive coupling includes terms of the form $e^{i\Omega t} \gamma^\dagger \gamma$. The physics in this regime can be understood as follows: two atoms in the condensate share the energy of a single photon and get kicked out of the condensate by the drive. The associated rate of energy absorption is related to the density of states of two-quasiparticle excitations at Ω . Specifically, if the non-driven system has quasiparticle excitations at energy $E_{\mathbf{k}}, E_{-\mathbf{k}}$ such that $\Omega = E_{\mathbf{k}} + E_{-\mathbf{k}}$, then energy absorption will occur and the system will be unstable. On the other hand, if $\Omega \geq 2W$, where $W \approx 2zJ_0$ is the approximate bandwidth of Bogoliubov excitations, then absorption does not occur and the system is stable.

Combining the insights from these two limits allows us to understand the entire stability phase diagram. The drive both renormalizes the bandwidth and creates pairs of *renormalized* Bogoliubov quasiparticles, which have a bandwidth $W_{\text{eff}} \approx 2zJ_{\text{eff}}(\zeta)$. More precisely, we can define $W_{\text{eff}} \equiv \max_k(E_{\text{eff}}(\mathbf{k})) - \min_k(E_{\text{eff}}(\mathbf{k}))$ as the effective Floquet-Bogoliubov bandwidth; in terms of this, the stability condition reads

$$\Omega_c > 2W_{\text{eff}} \Leftrightarrow \text{stable}, \quad (4)$$

Eq. (4) is consistent with our numerical results (Fig. 1). This result is unexpected at first sight, since the time-averaged Hamiltonian is valid at infinite frequency whereas parametric resonance is inherently a low-frequency phenomenon. One can understand our result as follows: the hopping matrix element in the driven system can be expanded as $J(t) \sim J_0 \sum_n \mathcal{J}_n(\zeta) \exp(in\Omega t)$. We can absorb the time-independent $n = 0$ component in the unperturbed Hamiltonian, and treat the $n = 1$ term, which oscillates at Ω , perturbatively. The smallness of this perturbation is guaranteed at $U \ll \Omega$, because the matrix element for creating two quasiparticles is proportional to both $\mathcal{J}_1(\zeta)$ [which need not be small] and U [which is assumed to be small]. This allows us to use the Golden Rule with the renormalized dispersion, and hence to conclude that a parametric instability takes place when $\Omega = 2W_{\text{eff}}$. In the limit $\Omega/J_0 \gg 1$, we obtain the analytic expression for the critical driving frequency

$$\Omega_c(\zeta) = 4\sqrt{zJ_{\text{eff}}(\zeta)(zJ_{\text{eff}}(\zeta) + n_0U)} \quad (5)$$

If in addition $\zeta, U/J_0 \ll 1$, we find the simple formula $\Omega_c(\zeta) = zJ_0(4 - \zeta^2) + 2n_0U$. The continuous behaviour as $U \rightarrow 0$, which suggests that any U , no matter how small,

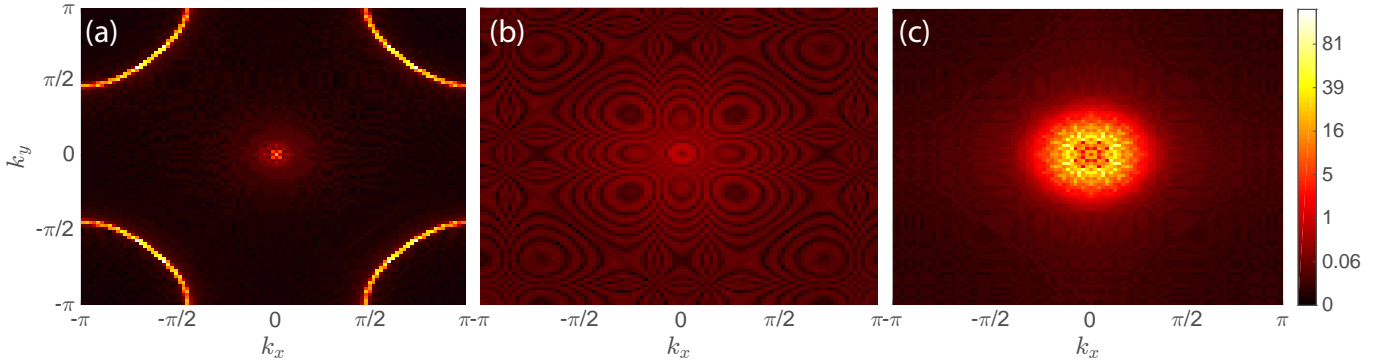


FIG. 3: (Color online). Snapshot of the momentum distribution $n_{\mathbf{k}} = \langle b_{\mathbf{k}}^\dagger b_{\mathbf{k}} \rangle - n_0$ after 801 driving cycles starting from a Bogoliubov initial state localised at $\mathbf{k} = \mathbf{0}$ for $U/J_0 = 0.2$. Panel (a) is in the unstable regime where the condensate is depleted due to parametric resonance. The bosons are excited by the drive to the quasienergy surface $\Omega = 2E_{\text{eff}}(k)$ (bright yellow-white circle around $\mathbf{k} = \pi$) where they occupy sharp peaks (white pixels). Panel (b) is in the regime where the condensate is stable on the pre-thermal timescales. In panel (c), the system is dynamically unstable due to the dispersion being inverted. The bright disc of excitations around $\mathbf{k} = \mathbf{0}$ corresponds to dynamically unstable modes. The parameters are (a) $\Omega/J_0 = 10$, $\zeta = 0.8$, (b) $\Omega/J_0 = 18$, $\zeta = 2.2$, and (c) $\Omega/J_0 = 20$, $\zeta = 3.8$.

can potentially lead to an instability for small enough frequencies.

Note that in the present case, resonant absorption occurs for drive strengths up to *twice* the single-particle bandwidth; by contrast, in noninteracting systems, no absorption occurs when Ω exceeds the single-particle bandwidth. The presence of absorption at frequencies exceeding the single-particle bandwidth is generic in interacting systems: in the most general case, n -particle absorption will be present for drive strengths less than the (renormalized) n -particle bandwidth; this can impose new constraints on the convergence properties of inverse-frequency expansions in systems featuring collective excitations⁴³. These n -particle processes appear, however, at parametrically large times (J_0/U)ⁿ and are absent in the WCCA. The discussion of time scales beyond the WCCA is deferred to App. C.

Condensate evolution.—Figure 2 [panel (a)] shows the evolution of the condensate fraction in the various regimes. In the unstable regime (solid blue line) the condensate fraction slowly decays with time. The decay rate [panel (b)] depends not only on drive strength ζ , but also on U and Ω —which together determine the matrix element for pair creation at the resonant momenta. By contrast, in the stable regime (dashed red line) the condensate quickly approaches its prethermal steady state value. In general, this can be lower than the Bogoliubov value, especially in the narrow-bandwidth regime $\zeta \lesssim 2.4$, since $|J_{\text{eff}}(\zeta)| < |J_0|$. Finally, when the initial state has an unstable condensate at a band maximum (dash-dotted black line), the condensate fraction once again decays. Very close to the region $\zeta \sim 2.405$ (grey strip in Fig. 1), the WCCA gives strong oscillations of the particle density between the condensates at $\mathbf{0}$ and π (see App. D); however, as previously noted, the WCCA is not reliable in this regime.

(Quasi-)momentum distribution.—Fig. 3 plots snap-

shots of the quasimomentum (i.e., lattice momentum) distribution after 801 driving cycles; the time evolution of this quantity is shown in App. F. Specifically, the quantity plotted is $n_{\mathbf{k}} = \langle b_{\mathbf{k}}^\dagger b_{\mathbf{k}} \rangle - n_0$, i.e., the condensate peak is subtracted out. The quasimomentum distribution can be directly accessed through band-mapping followed by time-of-flight imaging. Moreover, as we are concerned with a single-band model, it should be possible to extract this distribution directly from time-of-flight imaging, by focusing on momenta within the first Brillouin zone.

Figure 3 (a) shows the case in which the condensate is parametrically unstable. Here, as we expect, quasiparticles are strongly excited around the quasimomentum surface $\{\mathbf{k} : \Omega = 2E_{\text{eff}}(\mathbf{k})\}$ matching the resonance condition. Within Bogoliubov theory, the (time-averaged) excitation intensity should be uniform along this surface. However, as the points along this surface are not symmetry-related, the nonlinearities included in the WCCA should in general favor some points on the excitation surface over others. This is indeed what is seen numerically: while the entire surface is excited, some points have higher intensity than others (cf. white pixels in Fig. 3 (a)).

Figure 3 (b) shows the case in which the condensate is *stable*. Here, by contrast with panel (a), the quasiparticle population remains low throughout the Brillouin zone. From Bogoliubov theory, one would expect that bosonic modes satisfying $J_{\text{eff}}(\mathbf{k}) \lesssim U$ should have appreciable occupation in the steady state; this region should expand to cover more and more of the Brillouin zone as one moves toward the “Mott insulator” regime at $\zeta \approx 2.405$. The intricate patterns in momentum space arise as a result of the abrupt turn-on of the drive—which initializes the Floquet-Bogoliubov quasiparticle states in a nonequilibrium initial condition—and are absent when the drive is instead gradually ramped up. These patterns evolve nontrivially with time (see App. F).

Finally, Fig. 3 (c) illustrates the case in which the initial state is a condensate at $\mathbf{k} = \mathbf{0}$, but the dispersion is inverted ($\zeta > 2.4$) so that the only *stable* condensate is supported at $\mathbf{k} = \pi$. Thus the initial state is unstable regardless of the drive frequency. Let us consider the infinite-frequency limit; here, the situation we are considering amounts to a sudden quench of the single-particle dispersion. To explore the dynamics of this instability, we compute the Bogoliubov spectrum around a condensate at $\mathbf{k} = \mathbf{0}$ in an inverted dispersion. This computation yields that modes with momenta near $\mathbf{k} = \mathbf{0}$ acquire imaginary frequencies (and are thus unstable), whereas modes with large momenta are *stable*. [This might seem counterintuitive, as the larger-momentum modes have “more negative” energies; note, however, that in the $U \rightarrow 0$ limit, *all* modes are stable as there are no decay processes.] The unstable modes are determined by the condition $\varepsilon_{\text{eff}}(\mathbf{k}) + zJ_0 < 2n_0U$, where $\varepsilon_{\text{eff}}(\mathbf{k})$ is the single-particle Floquet dispersion of the Hamiltonian (3), and are dynamically stabilized in the course of the time evolution due to the nonlinear feedback of the self-consistent treatment⁴⁵. Our numerical results with the WCCA confirm this picture: the unstable modes at small quasimomenta acquire large populations, whereas the large-quasimomentum modes do not pick up quasiparticles. This behavior is *specific* to the WCCA, and in a real system it will correspond only to intermediate-time dynamics $t \lesssim J_0/U^2$. On longer times, collisions between quasiparticles should cause large occupation numbers across the Brillouin zone, see App. C.

Conclusion and Outlook.—In summary, we studied the instabilities and steady states in the periodically driven Bose-Hubbard model on a square lattice using the WCCA. We found that, whenever the driving frequency is larger than twice the effective bandwidth of the Floquet-Bogoliubov dispersion, the system is in a stable phase, corresponding to a pre-thermalised state. Consequently, in the high-frequency limit, the stability region is enhanced due to the decreased effective bandwidth. In the stable regime, the condensate fraction and the momentum distribution remain close to those of the initial state and the system does not absorb energy from the drive. Depending on the value of the driving strength ζ , we identified stable regions for states featuring a macroscopic occupation of the $\mathbf{k} = \mathbf{0}$ and $\mathbf{k} = \pi$ modes, respectively. By contrast, whenever $\Omega < 2W_{\text{eff}}$, the system is unstable due to resonant creation of pairs of Bogoliubov quasiparticles by the drive. The condensate fraction decays with the depletion rate increasing from the stability boundary inwards, and the (quasi-)momentum distribution exhibits sharp peaks corresponding to strong population of specific modes lying on the equipotential surface $\Omega = 2E_{\text{eff}}(\mathbf{k})$. The total energy of the system increases

due to resonant absorption from the drive and the system heats up (see App. E).

The main experimental prediction of this work—a parametric change in the heating rates as a function of the drive amplitude and frequency—is straightforward to measure in present-day experiments with Rb atoms, which are naturally in the weak-coupling regime. For the experiment in Ref. 20 the parameters were chosen as $U/J_0 \approx 0.1$, $\Omega/J_0 \approx 20$, and $\zeta \approx 0.6$, which is within the regime we considered. Although we focused on the case of a square lattice, the arguments directly generalize to other lattices, such as the honeycomb lattice, in which topologically non-trivial states can be stabilized. In contrast to the simulation of artificial gauge fields using Raman lasers^{13,14,16,20}, topological gaps in *mechanically shaken* optical lattices scale as Ω^{-1} .¹⁷⁻¹⁹ Hence, in order to engineer topological insulators with large gaps (and a large region of non-zero Berry curvature around them), it is desirable to go to lower frequencies. Our results impose a fundamental limit for *weakly-interacting bosonic* systems on how small the frequency can be, since for $\Omega < 2W_{\text{eff}}$ the system becomes unstable. More generally, our results suggest that conserving approximations, whether controlled by weak coupling or some other parameter as in large- N models⁴⁴⁻⁴⁹, are ways of exploring dynamical phase transitions in models that are both *interacting* (unlike free-particle models) and *finite-dimensional* (unlike the Kapitza pendulum or the kicked rotor). The critical properties of such phase transitions are a fruitful theme for future work. Although in practice such phase transitions will be smeared out by higher-order effects, the associated crossovers should still be experimentally observable.

Note added. As this work was nearing completion, a related work studying prethermalization in the driven, weakly interacting *Fermi-Hubbard* model appeared³¹. While this work also finds a transition between a stable (“prethermalized”) regime and a parametrically unstable (“Golden Rule”) regime, the underlying physics of Fermi- and Bose-Hubbard models, and therefore the phase diagrams, are quite different.

Acknowledgments. We thank D. Abanin, M. Babadi, I. Bloch, L. D’Alessio, E. Dalla Torre, M. Kolodrubetz, A. Polkovnikov, and U. Schneider for interesting and fruitful discussions. The authors acknowledge support from the NSF grant DMR-1308435, Harvard-MIT CUA, AFOSR New Quantum Phases of Matter MURI, the ARO-MURI on Atomtronics, ARO MURI Quism program, AFOSR FA9550-13-1-0039 and BSF 2010318, and Technische Universität München - Institute for Advanced Study, funded by the German Excellence Initiative and the European Union FP7 under grant agreement 291763.

* Electronic address: mbukov@bu.edu

¹ N. Goldman and J. Dalibard, Phys. Rev. X 4, 031027

(2014).

² M. Bukov, L. D'Alessio, and A. Polkovnikov, *Advances in Physics* **64**, 2 139226 (2015).

³ D. H. Dunlap and V. M. Kenkre, *Phys. Rev. B* **34**, 3625 (1986), *Phys. Rev. B* **37**, 6622 (1988).

⁴ A. Eckardt, C. Weiss, and M. Holthaus, *Phys. Rev. Lett.* **95**, 260404 (2005).

⁵ H. Lignier, C. Sias, D. Ciampini, Y. Singh, A. Zenesini, O. Morsch, and E. Arimondo, *Phys. Rev. Lett.* **99**, 220403 (2007).

⁶ A. Zenesini, H. Lignier, D. Ciampini, O. Morsch, and E. Arimondo, *Phys. Rev. Lett.* **102**, 100403 (2009).

⁷ C. E. Creffield, F. Sols, D. Ciampini, O. Morsch, and E. Arimondo, *Phys. Rev. A* **82**, 035601 (2010).

⁸ G. Jotzu, M. Messer, F. Görg, D. Greif, R. Desbuquois and T. Esslinger, arXiv:1504.05573 (2015).

⁹ J. Struck, C. Ölschläger, R. Le Targatn, P. Soltan- Panahi, A. Eckardt, M. Lewenstein, P. Windpassinger, and K. Sengstock, *Science* **333** (6045), 996-999 (2011).

¹⁰ D. Jaksch and P. Zoller, *Ann. Phys. (Amsterdam)* **315**, 52 (2003).

¹¹ E. J. Mueller, *Phys. Rev. A* **70**, 041603 (2004).

¹² J. Struck, M. Weinberg, C. Ölschläger, P. Windpassinger, J. Simonet, K. Sengstock, R. Höppner, P. Hauke, A. Eckardt, M. Lewenstein, and L. Mathey, *Nature Physics* **9**, 738-743 (2013).

¹³ M. Aidelsburger, M. Atala, M. Lohse, J. T. Barreiro, B. Paredes, and I. Bloch, *Phys. Rev. Lett.* **111**, 185301 (2013).

¹⁴ H. Miyake, G. A. Siviloglou, C. J. Kennedy, W. C. Burton, and W. Ketterle, *Phys. Rev. Lett.* **111**, 185302 (2013).

¹⁵ M. Atala, M. Aidelsburger, M. Lohse, J. T. Barreiro, B. Paredes, I. Bloch, *Nature Physics* **10**, 588593 (2014).

¹⁶ C. J. Kennedy, W. C. Burton, W. Ch. Chung, and W. Ketterle, arXiv:1503.08243 (2015).

¹⁷ T. Oka and H. Aoki, *Phys. Rev. B* **79** 081406(R), (2009).

¹⁸ T. Kitagawa, T. Oka, A. Brataas, L. Fu, and E. Demler, *Phys. Rev. B* **84** 235108, (2011).

¹⁹ G. Jotzu, M. Messer, R. Desbuquois, M. Lebrat, T. Uehlinger, D. Greif, and T. Esslinger, *Nature* **515**, 237 (2014).

²⁰ M. Aidelsburger, M. Lohse, C. Schweizer, M. Atala, J. T. Barreiro, S. Nascimbène, N. R. Cooper, I. Bloch, and N. Goldman, *Nature Physics* **11** 162166, (2015).

²¹ N. H. Lindner, G. Refael and V. Galitski, *Nature Physics* **7**, 490 (2011).

²² M. S. Rudner, N. H. Lindner, E. Berg, and M. Levin, *Phys. Rev. X* **3**, 031005 (2013).

²³ J. M. Deutsch, *Phys. Rev. A* **43**, 2046 (1991).

²⁴ M. Srednicki, *Phys. Rev. E* **50**, 888 (1994).

²⁵ M. Rigol, V. Dunjko, and M. Olshanii, *Nature (London)* **452**, 854 (2008).

²⁶ L. D'Alessio and A. Polkovnikov, *Annals of Physics* **333**, 19-33 (2013).

²⁷ L. D'Alessio and M. Rigol, *Phys. Rev. X* **4**, 041048 (2014).

²⁸ P. Ponte, Z. Papić, F. Huveneers and D. A. Abanin, *Phys. Rev. Lett.* **114**, 140401 (2015).

²⁹ D. Abanin, W. De Roeck, and F. Huveneers, arXiv:1507.01474 (2015).

³⁰ J. Berges, et al. *Phys. Rev. Lett.* **93**, 142002 (2004).

³¹ E. Canovi, M. Kollar, and M. Eckstein, arXiv:1507.00991 (2015).

³² M. Bukov, and A. Polkovnikov, *Phys. Rev. A* **90**, 043613 (2014).

³³ J. M. Cornwall, R. Jackiw and E. Tomboulis, *Phys. Rev. D* **10**, 8 (1974).

³⁴ P. C. Hohenberg and P. C. Martin, *Ann. Phys. (N.Y.)* **34**, 291 (1965).

³⁵ A. Griffin, *Phys. Rev. B* **53**, 9341 (1996).

³⁶ A. M. Rey, B. L. Hu, E. Calzetta, A. Roura, and C. W. Clark, *Phys. Rev. A* **69**, 033610 (2004).

³⁷ C. E. Creffield, *Phys. Rev. A* **79**, 063612 (2009).

³⁸ C. Zhang, J. Liu, M. G. Raizen, and Q. Niu, *Phys. Rev. Lett.* **92**, 5 (2004).

³⁹ S. Choudhury, E. J. Mueller, *Phys. Rev. A* **91**, 023624 (2015).

⁴⁰ T. Bilitewski and N. R. Cooper, *Phys. Rev. A* **91**, 063611 (2015).

⁴¹ B. Capogrosso-Sansone, S. Günes Sýler, N. Prokofev, and B. Svistunov, *Phys. Rev. A* **77**, 015602 (2008).

⁴² M. Knap, E. Arrigoni, and W. von der Linden, *Phys. Rev. B* **81**, 024301 (2010).

⁴³ A. Eckardt, and E. Anisimovas, arXiv:1502.06477v3, (2015).

⁴⁴ J. Bauer, M. Babadi, and E. Demler, arXiv:1411.4049 (2014).

⁴⁵ M. Babadi, E. Demler, and M. Knap, arXiv:1504.05956, (2015).

⁴⁶ M. Moshe and J. Zinn-Justin, *Phys. Rep.* **385**, 69 (2003).

⁴⁷ B. Sciolla and G. Biroli, *Phys. Rev. B* **88**, 201110(R) (2013).

⁴⁸ P. Smacchia, M. Knap, E. Demler, and A. Silva, *Phys. Rev. B* **91**, 205136 (2015).

⁴⁹ A. Chandran and S. L. Sondhi, arXiv:1506.08836, (2015).

⁵⁰ A. Kamenev, *Field Theory of Non-Equilibrium Systems*, Cambridge University Press (2011).

⁵¹ J. Berges, *AIP Conf. Proc.* **739**, 3-62 (2005).

⁵² M. Greiner, O. Mandel, T. W. Hänsch, and I. Bloch, *Nature* **419**, 51-54 (2002).

Appendix A: Transformation to the Rotating Frame

In this appendix, we discuss the transformation of the driven BHM from the lab frame to the rotating frame, i.e., from Eq. (1) to Eq. (2). The rotating frame is defined by the unitary transformation

$$V(t) = \exp \left(-i \left[\int_0^t \mathbf{E}(t') dt' + \mathcal{A}(0) \right] \cdot \sum_j \mathbf{r}_j n_j \right), \quad |\psi_{\text{rot}}(t)\rangle = V(t) |\psi_{\text{lab}}(t)\rangle, \quad b_j \rightarrow b_j e^{-i\mathcal{A}(t) \cdot \mathbf{r}_j}, \quad (\text{A1})$$

where $\mathcal{A}(t) = \zeta (\sin \Omega t, -\cos \Omega t)^T$. This time-dependent change of basis is equivalent to the standard gauge transformation in electromagnetism $\mathbf{E}(t) \sim \partial_t \mathcal{A}(t)$. Physically, the transformation trades the fast time-dependence of

the quasimomentum for a time oscillating dispersion relation. The infinite-frequency limit is non-trivial when the amplitude of the gauge potential $\zeta = A/\Omega$ remains finite. This rotation facilitates the analytic computation the time-averaged Floquet Hamiltonian. In fact, going to the rotating frame is equivalent to re-summing an infinite inverse-frequency subseries in the lab-frame². As a result, the effective hopping matrix element is a non-perturbative function of ζ .

Appendix B: Derivation of the equations of motion within the Weak-Coupling Conserving Approximation

In this appendix, we derive the equations of motion (EOM) using the weak-coupling conserving approximation (WCCA). We are interested in studying the periodically driven Bose-Hubbard model on a 2D lattice:

$$H(t) = - \sum_{ij} J_{ij}(t) b_i^\dagger b_j + \text{h.c.} + \frac{U}{2} \sum_j n_j(n_j - 1), \quad (\text{B1})$$

In order to treat the spontaneous symmetry breaking of the condensate efficiently, we introduce the Bogoliubov spinor for the bosonic fields $b \rightarrow b_a$, with $a = 1, 2$, where $b_1 = b$ and $b_2 = b^*$. Adopting the notation $(j, t) = x$, the time-dependent action can be cast into the compact form

$$\begin{aligned} S[b, b^*] &= S_0 + S_{\text{int}} \\ S_0[b, b^*] &= \frac{1}{2} \int_C dx b_a^*(x) \left(G_{\text{free}}^{(-1)} \right)_{ab} (x, y) b_b(y) \\ S_{\text{int}}[b, b^*] &= -\frac{U}{2} \int_C dx dy \delta_C(x - y) b^*(x) b^*(x) b(x) b(x). \end{aligned} \quad (\text{B2})$$

where the integral over time is taken along the Keldysh roundtrip contour $C^{33,50,51}$ and we introduced the delta function $\delta_C(x - x') = \delta_C(t - t')\delta_{jj'}$. In Bogoliubov space, the noninteracting Green's function has thus the form

$$\left(G_{\text{free}}^{(-1)} \right)_{ab} = \begin{pmatrix} i\partial_t + J_{ij}(t) & 0 \\ 0 & -i\partial_t + J_{ij}^*(t) \end{pmatrix}_{ab}. \quad (\text{B3})$$

We define the vacuum expectation value (VEV) $\varphi(x)$ and the quasiparticle (phonon) propagator $G(x, y)$ as

$$\varphi_a(x) = \langle b_a(x) \rangle, \quad iG_{ab}(x, y) = \langle b_a(x) b_b^*(y) \rangle_c = \begin{pmatrix} \langle \tilde{b}(x) \tilde{b}^*(y) \rangle_c & \langle \tilde{b}(x) \tilde{b}(y) \rangle_c \\ \langle \tilde{b}^*(x) \tilde{b}^*(y) \rangle_c & \langle \tilde{b}^*(x) \tilde{b}(y) \rangle_c \end{pmatrix}. \quad (\text{B4})$$

The microscopically occupied fields are denoted with a tilde $\tilde{b}(x)$. Hence the Green's function G defined above does *not* include the condensate fraction. The effective action is given by the double Legendre transform of the original action w.r.t. the VEV $\varphi(x)$ and the correlator $G_{ab}(x, y)$ ^{33,51}:

$$\begin{aligned} \Gamma[\varphi, G] &= S[\varphi, \varphi^*] + \frac{1}{2} \text{Tr}[\log G^{-1}] + \frac{1}{2} \text{Tr}[G_0^{-1}(\varphi)G] - \Gamma_2[\varphi, G], \\ S[\varphi, \varphi^*] &= \int dx dy \varphi^*(x) G_{\text{free}}^{-1}(x, y) \varphi(y) - \frac{U}{2} \int dx |\varphi(x)|^4 \equiv \int dx dy \varphi^*(x) G_0^{-1}(x, y; \varphi) \varphi(y), \end{aligned} \quad (\text{B5})$$

where the sum over the Bogoliubov-Nambu index a is implicit. The Bogoliubov propagator $G_0^{-1}(x, y; \varphi)$ generates the motion of the Gross-Pitaevskii equation. Notice that it depends on the field φ itself since the GPE is nonlinear. From that we obtain the inverse Bogoliubov propagator $(G_0^{-1})_{ab}(x, y; \varphi)$ via:

$$\frac{1}{2} (G_0^{-1})_{ab}(x, y; \varphi) = \frac{\delta^2 S[\varphi, \varphi^*]}{\delta \varphi_a^*(x) \delta \varphi_b(y)} = \frac{1}{2} (G_{\text{free}}^{-1})_{ab}(x, y) - \frac{U}{2} \delta_C(x - y) \begin{pmatrix} 2|\varphi(x)|^2 & \varphi(x)^2 \\ (\varphi(x)^*)^2 & 2|\varphi(x)|^2 \end{pmatrix}_{ab}. \quad (\text{B6})$$

So far the calculation is exact, however, we have not specified the Luttinger-Ward functional $\Gamma_2[\varphi, G]$ yet which is the sum of all two-particle irreducible diagrams and thus has to be treated approximately. Here, we consider a weak-coupling expansion which amounts to consider diagrams to first order in U , see Fig. 4.

$$2 \times -i \frac{U}{2} \times 2 \int d^4x G_{11}(x,x) G_{22}(x,x)$$

$$-i \frac{U}{2} (i)^2 \times \int d^4x G_{12}(x,x) G_{21}(x,x)$$

FIG. 4: All two-particle irreducible diagrams which enter Γ_2 to first order in U , with their proper combinatorial factors. The diagrams can be turned into equations using the following Feynman rules: (i) a factor of $-iU/2$ for each vertex, and (ii) a factor of i for each closed loop. By symmetry $G_{11} = G_{22}$ and $G_{12} = (G_{21})^*$.

The EOM for the VEV and the propagator are obtained by making the effective action Γ stationary with respect to the fields, $\frac{\delta\Gamma[\varphi,G]}{\delta\varphi^*} = 0$ and $\frac{\delta\Gamma[\varphi,G]}{\delta G_{ab}} = 0$, which lead to:

$$\int_C dy (G_{\text{free}}^{-1})_{11}(x,y) \varphi(y) - U \varphi^*(x) \varphi^2(x) - U (2\varphi(x) G_{11}(x,x) + \varphi^*(x) G_{12}(x,x)) = 0,$$

$$\sum_b \left[(G_{\text{free}}^{-1})_{ab}(t) - U \delta_C(x-y) \begin{pmatrix} 2(iG_{11} + |\varphi|^2) & iG_{12} + \varphi^2 \\ iG_{21} + (\varphi^*)^2 & 2(iG_{22} + |\varphi|^2) \end{pmatrix}_{ab} \right] G_{bc}(t,t') = \delta_{ac} \delta_C(t-t'), \quad (\text{B7})$$

and the Green's function multiplication in the second equation above is understood in the matrix-multiplication sense: $(AB)(x,z) = \int_y A(x,y)B(y,z)$. We remark that these EOM are equivalent to the Bogoliubov-Hartree-Fock EOM derived in Ref. 35 when starting from the Hamiltonian (2), making the ansatz $b_{k=0} = \varphi + \tilde{b}_{k=0}$, $b_{k\neq 0} = \tilde{b}_{k\neq 0}$, and then linearises any cubic terms in \tilde{b}_k .

Next, we open the closed time contour⁵¹ by decomposing the Green's function into a spectral part $\rho(x,y)$ and a statistical part $F(x,y)$ according to

$$iG(x,x') = F(x,x') - \frac{i}{2} \rho(x,x') \text{sgn}_C(t-t'),$$

$$F_{ab}(x,x') = \frac{1}{2} \langle \{b_a(x), b_b^\dagger(x')\} \rangle_c = \frac{1}{2} \begin{pmatrix} \langle \{\tilde{b}(x), \tilde{b}^\dagger(x')\} \rangle & \langle \{\tilde{b}(x), \tilde{b}(x')\} \rangle \\ \langle \{\tilde{b}^\dagger(x), \tilde{b}^\dagger(x')\} \rangle & \langle \{\tilde{b}^\dagger(x), \tilde{b}(x')\} \rangle \end{pmatrix}_{ab}$$

$$\rho_{ab}(x,x') = i \langle [b_a(x), b_b^\dagger(x')] \rangle_c = i \begin{pmatrix} \langle [\tilde{b}(x), \tilde{b}^\dagger(x')] \rangle & \langle [\tilde{b}(x), \tilde{b}(x')] \rangle \\ \langle [\tilde{b}^\dagger(x), \tilde{b}^\dagger(x')] \rangle & \langle [\tilde{b}^\dagger(x), \tilde{b}(x')] \rangle \end{pmatrix}_{ab} \quad (\text{B8})$$

The following relations follow immediately from the above definitions:

$$F_{12}(x,x') = F_{12}(x',x), \quad \rho_{12}(x,x') = -\rho_{12}(x',x),$$

$$F_{21}(x,x') = F_{21}(x',x), \quad \rho_{21}(x,x') = -\rho_{21}(x',x),$$

$$F_{12}(x,x') = F_{21}^*(x,x'), \quad \rho_{12}(x,x') = \rho_{21}^*(x,x'),$$

$$F_{11}(x,x') = F_{11}^*(x',x), \quad \rho_{11}(x,x') = -\rho_{11}^*(x',x),$$

$$F_{22}(x,x') = F_{22}^*(x,x'), \quad \rho_{22}(x,x') = \rho_{22}^*(x,x'). \quad (\text{B9})$$

We now assume that the system is translationally invariant, with periodic boundary conditions. We find the following system of coupled nonlinear EOM in momentum space for the condensate

$$i\partial_t \varphi(t) = (zJ_0 - \mu)\varphi(t) + \varepsilon_{k=0}(t)\varphi(t) + \frac{U}{N_s} \left[[\varphi(t)]^* [\varphi(t)]^2 + 2\varphi(t) \int_q F_{11}(t,t;q) + [\varphi(t)]^* \int_q F_{12}(t,t;q) \right], \quad (\text{B10})$$

and the statistical correlator F

$$\begin{aligned} i\partial_t F_{11}(t, t'; k) &= (zJ_0 - \mu)F_{11}(t, t'; k) + \varepsilon_k(t)F_{11}(t, t'; k) \\ &\quad + \frac{U}{N_s} \left[2 \left(|\varphi(t)|^2 + \int_q F_{11}(t, t; q) \right) F_{11}(t, t'; k) + \left([\varphi(t)]^2 + \int_q F_{12}(t, t; q) \right) [F_{12}(t, t'; k)]^* \right], \\ i\partial_t F_{12}(t, t'; k) &= (zJ_0 - \mu)F_{12}(t, t'; k) + \varepsilon_k(t)F_{12}(t, t'; k) \\ &\quad + \frac{U}{N_s} \left[2 \left(|\varphi(t)|^2 + \int_q F_{11}(t, t; q) \right) F_{12}(t, t'; k) + \left([\varphi(t)]^2 + \int_q F_{12}(t, t; q) \right) [F_{11}(t, t'; k)]^* \right]. \end{aligned} \quad (\text{B11})$$

For completeness, we also give the equations of motion for the spectral correlators ρ which, on the other hand, obey

$$\begin{aligned} i\partial_t \rho_{11}(t, t'; k) &= (zJ_0 - \mu)\rho_{11}(t, t'; k) + \varepsilon_k(t)\rho_{11}(t, t'; k) \\ &\quad + \frac{U}{N_s} \left[2 \left(|\varphi(t)|^2 + \int_q F_{11}(t, t; q) \right) \rho_{11}(t, t'; k) + \left([\varphi(t)]^2 + \int_q F_{12}(t, t; q) \right) [\rho_{12}(t, t'; k)]^* \right], \\ i\partial_t \rho_{12}(t, t'; k) &= (zJ_0 - \mu)\rho_{12}(t, t'; k) + \varepsilon_k(t)\rho_{12}(t, t'; k) \\ &\quad + \frac{U}{N_s} \left[2 \left(|\varphi(t)|^2 + \int_q F_{11}(t, t; q) \right) \rho_{12}(t, t'; k) + \left([\varphi(t)]^2 + \int_q F_{12}(t, t; q) \right) [\rho_{11}(t, t'; k)]^* \right]. \end{aligned} \quad (\text{B12})$$

In the above equations, z is the coordination number, $\varepsilon_k(t)$ is the time-periodic free dispersion in the rotating frame, cf. App A, and the integrals are all taken over the Brillouin zone.

Furthermore, if one is interested in the equal-time correlation of the statistical correlator F , using the symmetry relations in Eq. (B9) one arrives at the somewhat simplified equations

$$\begin{aligned} \partial_t F_{11}(t, t; k) &= 2\text{Im} \left\{ \frac{U}{N_s} \left([\varphi(t)]^2 + \int_q F_{12}(t, t; q) \right) [F_{12}(t, t; k)]^* \right\}, \\ i\partial_t F_{12}(t, t; k) &= 2 \left\{ (zJ_0 - \mu)F_{12}(t, t; k) + \varepsilon_k(t)F_{12}(t, t; k) \right. \\ &\quad \left. + \frac{U}{N_s} \left[2 \left(|\varphi(t)|^2 + \int_q F_{11}(t, t; q) \right) F_{12}(t, t; k) + \left([\varphi(t)]^2 + \int_q F_{12}(t, t; q) \right) [F_{11}(t, t; k)]^* \right] \right\}. \end{aligned} \quad (\text{B13})$$

1. WCCA Equations of Motion for the BHM on a General Bipartite Lattice

We now generalise the WCCA EOM to any bipartite lattice. Consider a bipartite lattice with the two sublattices labelled by A and B and periodic boundary conditions. Each sublattice contains $N_A = N_B = N_s/2$ number of sites. With this definition, additionally to the Bogoliubov index $a = 1, 2$, all correlators carry an additional index $\alpha = A, B$, and so does the condensate fraction.

The extended system of equal-time equations of motion for the WCCA of the BHM reads

$$\begin{aligned} i\partial_t \varphi^A(t) &= (zJ_0 - \mu)\varphi^A(t) + \varepsilon_{k=0}(t)\varphi^B(t) \\ &\quad + \frac{U}{N_A} \left[[\varphi^A(t)]^* [\varphi^A(t)]^2 + 2\varphi^A(t) \int_q F_{11}^{AA}(t, t; q) + [\varphi^A(t)]^* \int_q F_{12}^{AA}(t, t; q) \right], \\ i\partial_t \varphi^B(t) &= (zJ_0 - \mu)\varphi^B(t) + \varepsilon_{k=0}(t)\varphi^A(t) \\ &\quad + \frac{U}{N_A} \left[[\varphi^B(t)]^* [\varphi^B(t)]^2 + 2\varphi^B(t) \int_q F_{11}^{BB}(t, t) + [\varphi^B(t)]^* \int_q F_{12}^{BB}(t, t) \right], \end{aligned} \quad (\text{B14})$$

$$\begin{aligned}
\partial_t F_{11}^{AA}(t, t; k) &= 2\text{Im} \left\{ \varepsilon_k(t) [F_{11}^{AB}(t, t; k)]^* + \frac{U}{N_A} \left([\varphi^A(t)]^2 + \int_q F_{12}^{AA}(t, t; q) \right) [F_{12}^{AA}(t, t; k)]^* \right\}, \\
\partial_t F_{11}^{BB}(t, t; k) &= 2\text{Im} \left\{ \varepsilon_k^*(t) F_{11}^{AB}(t, t; k) + \frac{U}{N_A} \left([\varphi^B(t)]^2 + \int_q F_{12}^{BB}(t, t; q) \right) [F_{12}^{BB}(t, t; k)]^* \right\}, \\
i\partial_t F_{11}^{AB}(t, t; k) &= \varepsilon_k(t) (F_{11}^{BB}(t, t; k) - F_{11}^{AA}(t, t; k)) + \frac{U}{N_A} \left[\right. \\
&\quad \left. + 2 \left(|\varphi^A(t)|^2 - |\varphi^B(t)|^2 + \int_q F_{11}^{AA}(t, t; q) - F_{11}^{BB}(t, t; q) \right) F_{11}^{AB}(t, t; k) \right. \\
&\quad \left. + \left([\varphi^A(t)]^2 + \int_q F_{12}^{AA}(t, t; q) \right) [F_{12}^{AB}(t, t; k)]^* - \left([\varphi^B(t)]^2 + \int_q F_{12}^{BB}(t, t; q) \right) [F_{12}^{AB}(t, t; k)]^* \right], \\
i\partial_t F_{12}^{AA}(t, t; k) &= 2 \left\{ (zJ_0 - \mu) F_{12}^{AA}(t, t; k) + \varepsilon_k(t) F_{12}^{BA}(t, t; k) \right. \\
&\quad \left. + \frac{U}{N_A} \left[2 \left(|\varphi^A(t)|^2 + \int_q F_{11}^{AA}(t, t; q) \right) F_{12}^{AA}(t, t; k) + \left([\varphi^A(t)]^2 + \int_q F_{12}^{AA}(t, t; q) \right) [F_{11}^{AA}(t, t; k)]^* \right] \right\}, \\
i\partial_t F_{12}^{BB}(t, t; k) &= 2 \left\{ \varepsilon_k^*(t) F_{12}^{AB}(t, t; k) + (zJ_0 - \mu) F_{12}^{BB}(t, t; k) \right. \\
&\quad \left. + \frac{U}{N_A} \left[2 \left(|\varphi^B(t)|^2 + \int_q F_{11}^{BB}(t, t; q) \right) F_{12}^{BB}(t, t; k) + \left([\varphi^B(t)]^2 + \int_q F_{12}^{BB}(t, t; q) \right) [F_{11}^{BB}(t, t; k)]^* \right] \right\}, \\
i\partial_t F_{12}^{AB}(t, t; k) &= 2(zJ_0 - \mu) F_{12}^{AB}(t, t; k) + (\varepsilon_k(t)^* F_{12}^{AA}(t, t; k) + \varepsilon_k(t) F_{12}^{BB}(t, t; k)) + \frac{U}{N_A} \left[\right. \\
&\quad \left. + 2 \left(|\varphi^A(t)|^2 + |\varphi^B(t)|^2 + \int_q F_{11}^{AA}(t, t; q) + F_{11}^{BB}(t, t; q) \right) F_{12}^{AB}(t, t; k) \right. \\
&\quad \left. + \left([\varphi^A(t)]^2 + \int_q F_{12}^{AA}(t, t; q) \right) [F_{11}^{AB}(t, t; k)]^* - \left([\varphi^B(t)]^2 + \int_q F_{12}^{BB}(t, t; q) \right) [F_{11}^{AB}(t, t; k)]^* \right]. \quad (\text{B15})
\end{aligned}$$

All integrals in Eqs. (B14) and (B15) are taken over the reduced Brillouin zone (w.r.t. the *AB*-sublattice symmetry). Equations (B14) and (B15) constitute a coupled set of non-linear equations, the solution of which produces the dynamics discussed in the main text. Note that these EOM can be applied to systems with arbitrary time-dependence (not necessarily a periodic one) and on an arbitrary bipartite lattice, such as the honeycomb lattice.

Appendix C: Validity of the WCCA and Thermalisation Timescales

In this Appendix we estimate the timescales on which the WCCA gives a reliable description of the physics, and discuss the dominant processes that (in the weak coupling regime) destabilize the various pre-thermal steady states discussed in the main text. We discuss each of the three regimes separately.

Parametrically unstable region. In this regime, the prethermalized phase is the one in which the momentum distribution is sharply peaked along momentum-space arcs as in Fig. 3 (a). As in the main text, we treat the time-averaged dispersion as the unperturbed Hamiltonian and look at the Golden Rule growth rate due to a perturbation of the form $J_0 \mathcal{J}_1(\zeta) b_{\mathbf{k}}^\dagger b_{\mathbf{k}}$. The matrix element for pair creation is then $\sim U n_0 \mathcal{J}_1(\zeta) / \mathcal{J}_0(\zeta)$ (assuming we are not too close to $\zeta = 2.4$), and for reasonably large drives this is of order U . Fermi's Golden Rule predicts that these features will grow at the rate $\Gamma \sim (U n_0)^2 / W_{\text{eff}}$, where n_0 is the condensate amplitude. The decay rate (i.e., inverse lifetime) of the quasiparticles along these arcs, once they are formed, is limited by collisions, and is also of order U^2 ; this is the rate at which these features spread out in momentum space. Thus there is no parametric separation in U between the formation and decay rate of these peaks. The leading collisional process comes from cubic terms of the form $U \varphi^* b_{\mathbf{k}_1}^\dagger b_{\mathbf{k}_2} b_{\mathbf{k}_1 - \mathbf{k}_2}$ (plus appropriate conjugates) in the Hamiltonian. The Golden Rule rate for this particular process is

$$\Gamma_c(\mathbf{k}) \sim U^2 n_0 n_{\mathbf{k}} \mathcal{N}_{2p}(E_{\text{eff}}(\mathbf{k})) \quad (\text{C1})$$

where $\mathcal{N}_{2p}(E_{\text{eff}}(\mathbf{k})) \sim \int dE' d^2q \delta(E' - E_{\text{eff}}(\mathbf{q})) \delta(E_{\text{eff}}(\mathbf{k}) - E' - E_{\text{eff}}(\mathbf{q} - \mathbf{k}))$ is the accessible two-particle density of states. Here, $E_{\text{eff}}(\mathbf{q})$ is the energy of an excitation with quasimomentum \mathbf{q} . On dimensional grounds this two-particle density of states must be inversely proportional to W_{eff} ; thus, the overall Golden Rule lifetime of a particular quasiparticle state will go as

$$\Gamma_c(\mathbf{k}) \sim U^2 n_0 n_{\mathbf{k}} / W_{\text{eff}} \quad (\text{C2})$$

up to a multiplicative constant. Thus the decay rate of a mode is slower than the creation rate whenever the condensate amplitude is large compared with the population of the mode (essentially because the matrix element is not Bose-enhanced to the same degree). At short times, when the condensate is not appreciably depleted, the WCCA is therefore reliable; however, when the depletion becomes large the WCCA also fails. Thus the regimes of validity of the WCCA and Bogoliubov theory in the parametrically unstable regime are essentially the same, although the WCCA has the advantage of respecting particle number conservation *exactly* at all times.

Stable region. In the stable region there are two types of physical processes beyond the WCCA. (1) The excitations created by the original quench into the phase have finite collisional lifetimes, as discussed above. The momentum-space patterns in the stable region will dephase on this Golden-Rule timescale Γ_c ; however, the condensate fraction will remain large and stable even after dephasing. (2) Eventually, the system will absorb energy from the drive. If the drive frequency is Ω and the bandwidth of single-particle excitations is W_{eff} , then resonant absorption must involve at least $m \equiv \Omega/W_{\text{eff}}$ quasiparticles. It is straightforward to check that the associated Golden Rule rate, at weak coupling, is of the form U^m/W_{eff}^{m-1} . When U is sufficiently small, this heating timescale is much longer than the timescale on which the momentum-space patterns dephase; thus the system should remain *stable* for extremely long times at high frequencies.

Dynamically unstable region. In this regime, the growth rates of unstable modes are of order U , whereas the collision rates are of order U^2/W_{eff} at best, so at weak coupling we have a linear parametric window in U where the WCCA remains valid.

Appendix D: Phase Transition Region around $\zeta = 2.405$

In this appendix, we discuss the dynamics governed by the WCCA close to the zero of the Bessel function, $\zeta = 2.405$, where the dispersion of the $\Omega \rightarrow \infty$ Hamiltonian becomes flat (central grey region in Fig. 1). For $\zeta < 2.405$ the dispersion of the free theory $U = 0$ supports a stable minimum for $\mathbf{k} = \mathbf{0}$, while for $\zeta > 2.405$ the stable minimum appears at $\mathbf{k} = \pi$. Since the two stable regions support different momentum modes, a phase transition occurs in between them. Therefore, it is required that one allows for a macroscopic population of both the modes in the immediate vicinity of $\zeta = 2.405$.

This can be achieved by reducing the translational symmetry of the problem. Intuitively, a condensate at $\mathbf{k} = \pi$ with amplitude $\varphi_{k=\pi}$ flips a sign on every other site. Hence, one can choose to work in the original (momentum-resolved) basis $(\varphi_{k=0}, \varphi_{k=\pi})$, or in the site-resolved basis (φ^A, φ^B) . The two are related by a rotation. In order to allow for a dynamical population of the $\varphi_{k=\pi}$ condensate, Eqs. (B14) and (B15) require that the initial condition for $\varphi_{\pi}(0) = 1/\sqrt{2}(\varphi^A(0) - \varphi^B(0))$ be nonzero. In the AB -basis, this is equivalent to saying that there is a slight difference in the condensate occupation on the two sublattices. Physically, this imbalance is caused by spontaneous symmetry breaking. However, in the WCCA one has to put in this imbalance by hand. In the following we refer to the small value $s = |\varphi_{\pi}(0)|^2$ as *seed*.

When the effective dispersion becomes flat $\zeta \approx 2.405$ [Fig 5], the condensate undergoes oscillations between the $\mathbf{0}$ and π modes, with a period $\sim 1/U$ for small U . This behaviour is reminiscent of the collapse-and-revival effects seen for a BEC that is suddenly quenched into the Mott insulating phase⁵², although the dynamics governed by WCCA is classical. The period of the transfer oscillations is also seed-dependent and increases with $s \rightarrow 0$. Even though our approximation does not capture a true Mott insulating phase, the nonlinearities included in the WCCA are sufficient to give rise to these oscillations. Physically speaking, a quasiparticle-mediated channel is opened, through which particles flow from the condensate at $\mathbf{k} = \mathbf{0}$ to $\mathbf{k} = \pi$. Although it is present at any ζ , this channel is only effective when the dispersion is sufficiently flat since the amplitude for the phonon-mediated transition $\varphi_{k=0} \rightarrow b_k^\dagger \rightarrow \varphi_{k=\pi}$ scales as $(U/J_0)^2$.

Appendix E: Time-Dependence of the Energy

Last, we briefly address the issue of heating. Fig. 6 shows the excess total (i.e., condensate plus quasiparticle) energy density in the system, relative to the non-driven state. Due to the abrupt turn-on of the periodic circularly

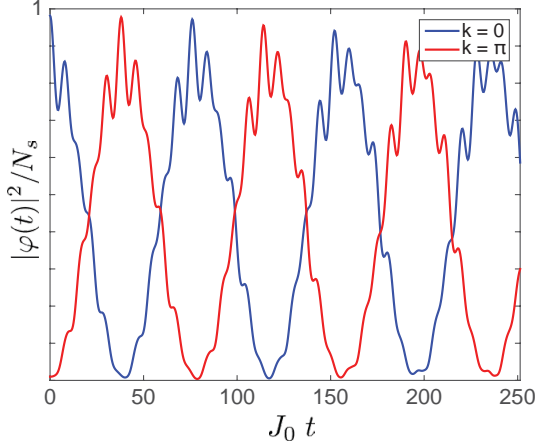


FIG. 5: Time evolution of the condensate fractions for $\zeta = 2.405$ and $\Omega/J_0 = 20$ starting from a Bogoliubov initial state localised at $\mathbf{k} = \mathbf{0}$. The seed size is $s = 1\%$ and $U/J_0 = 0.2$.

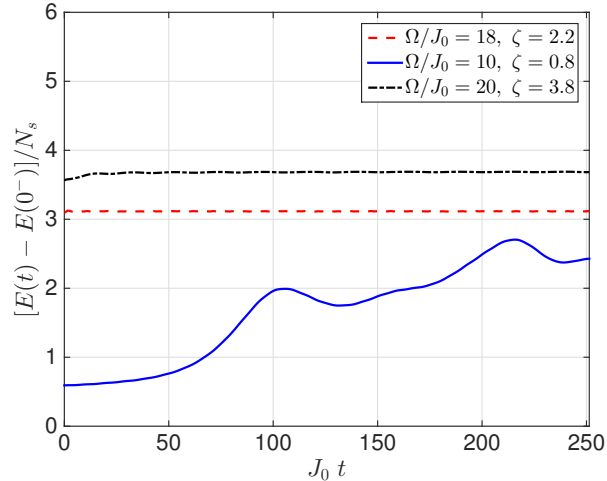


FIG. 6: Total energy density of condensate and quasiparticles as a function of time for $U/J_0 = 0.2$ following the quench with frequency and amplitude as stated in the legend.

polarised modulation, the energy changes discontinuously at $t = 0$. As expected, the energy density increases due to heating in the parametrically unstable region, saturates in the stable region, and exhibits a small growth for $\zeta \approx 3.8$. Notice the different behaviour in the parametrically unstable region compared to the dynamically unstable one: while in the former the energy grows due to the population of modes lying on the high-energy surface, in the latter the dynamically unstable modes appear close enough to the origin [cf. Fig. 3, panel (c)] so that the growth in energy density past the quench value is not substantial. Note that the system does not heat up even at fairly long times whenever the parameters are chosen to be in the stable region of the stability diagram. Although ergodic periodically-driven systems are expected to eventually heat up to infinite temperature^{26–28}, in the weak-coupling limit this heating timescale (which is due to collisions between quasiparticles) is parametrically slower in the “stable” regimes of our phase diagram than in the “unstable” regimes. Thus, for a range of present-day experiments, we expect that in the stable high-frequency regime there is no significant heating on experimentally relevant timescales.

Appendix F: Time-Dependence of the Momentum Distribution Function

For the time-evolution of the momentum distribution function, we refer to the three videos in the supplementary material. The lower left panel shows the quasiparticle momentum distribution over the first Brillouin zone, while the upper left panel is a top view of the same. The upper right panel displays the time-evolution of the condensate

fraction, while the lower right panel shows the energy density. The parameters for each simulation can be found in the title. The three movies correspond to the points in the stability diagram marked by (a), (b), (c) in Fig. 1.
